

Angular dependence of the interlayer coupling at the interface between two dimensional materials 1T-PtSe₂ and graphene

P. Mallet¹, F. Ibrahim², K. Abdukayumov², A. Marty², C. Vergnaud², F. Bonell², M. Chshiev², M. Jamet² and J-Y Veuille^{1,*}

¹ Univ. Grenoble Alpes, CNRS, Grenoble INP, Institut NEEL, 38000 Grenoble, France

² Univ. Grenoble Alpes, CEA, CNRS, Grenoble INP, IRIG-SPINTEC, 38000 Grenoble, France

* : jean-yves.veuille@neel.cnrs.fr

Abstract:

We present a study by Scanning Tunneling Microscopy, supported by ab initio calculations, of the interaction between graphene and monolayer (semiconducting) PtSe₂ as a function of the twist angle θ between the two layers. We analyze the PtSe₂ contribution to the hybrid interface states that develop within the bandgap of the semiconductor to probe the interaction. The experimental data indicate that the interlayer coupling increases markedly with the value of θ , which is confirmed by ab initio calculations. The moiré patterns observed within the gap are consistent with a momentum conservation rule between hybridized states, and the strength of the hybridization can be qualitatively described by a perturbative model.

Proximity effect allows transferring some electronic properties at the interface between two materials without dramatically affecting their individual structure. This phenomenon is thought to be especially relevant for few layers thick materials where even short range interactions can impact the properties of the whole sample [1]. Therefore, proximity effect represents an efficient strategy for tuning the properties of van der Waals heterostructures [2]. For instance, it has been exploited to imprint a spin dependent electronic structure in graphene when brought in contact with semi-conducting (SC) or insulating two dimensional (2D) layers exhibiting either strong spin-orbit coupling or magnetic ordering [1-4]. Inducing either a significant spin-orbit interaction [5-16] and/or a large magnetic exchange [17-25] in graphene is highly desired for developing spintronics based on 2D materials [1, 3, 4, 26, 27]. Considering the relevance of the proximity effect, it is crucial to determine which factors drive the strength of the coupling between a SC 2D layer and graphene. One important parameter is the rotation angle θ between the atomic lattices of the two layers. Recent theoretical studies [28-32] have indeed revealed that the amplitude and even the sign of the proximity effect can strongly depend on θ . Exploiting this angular dependence is the key aspect of the rapidly developing field of “twistronics” [33, 34].

In this work, we have investigated the basic mechanisms underlying the interaction between graphene and a SC 2D transition metal dichalcogenide (TMD) layer by means of scanning tunneling microscopy (STM) and spectroscopy (STS), complemented by ab initio simulations. Our approach consists in analyzing the electronic states that appear within the SC bandgap on the TMD side of the heterostructure as a consequence of the interfacial coupling. We thus probe the component in the PtSe₂ layer of the states formed within the TMD bandgap by hybridization with the low energy states of graphene. This includes the states close to the Dirac point (DP) of (bilayer) graphene, that is located around 0.3 eV below the Fermi level in the samples we use [35]. This hybridization is precisely the mechanism that generates the spin dependent proximity effect [1, 3, 4, 6, 17, 18, 28, 29, 31, 32], and our approach allows to probe it directly. We have analyzed domains corresponding to different values

of θ . Our data show evidence for the angular dependence of the interfacial coupling and support the perturbative model presented in Refs. 28, 29 and 36. Notice that our approach is different from the one reported recently [37], where the proximity effect was studied by probing quantum interference patterns from the graphene side.

As a SC TMD we have chosen monolayer (1L) PtSe₂, which has a bandgap of about 2 eV. 1T-PtSe₂ actually shows a comparatively large interlayer interaction in the TMD family [38, 39, 40]. If this property is preserved at the interface with graphene, it would lead to a large hybridization and thus to a detectable signal within the TMD bandgap in the STM measurements. Although we do not address this point, 1L PtSe₂ is also potentially interesting to induce spin dependent proximity effects in graphene, owing to a strong spin-orbit coupling [41, 42, 43] and to a long range defect-induced magnetic ordering [44].

The PtSe₂ layer was grown by molecular beam epitaxy (MBE) on a graphene bilayer substrate (BLG) grown on SiC [45]. The STM measurements were performed in a setup operating at 8.5K, and analyzed using the WSxM software [46]. Ab initio calculations were performed using the VASP package [47, 48; 49]. Technical details are found in Ref. 50.

Fig. 1-a and Fig. S1 [50] show that the sample surface is mostly covered by the monolayer PtSe₂ (1L PtSe₂) phase, with domains size of the order of 10 nm. Some patches of BLG substrate remain visible, and a few bilayer PtSe₂ islands (not discussed here) are also present. In many domains, the PtSe₂ lattice is almost aligned with the BLG (see section SI2 in Ref. [50]), as already reported in samples grown on Highly Ordered Pyrolytic Graphite (HOPG) [51, 52, 53]. This leads to a quasi-(2x2) superstructure in STM images, since twice the lattice constant of PtSe₂ (0.375 nm) is almost equal to three times the lattice constant of graphene (0.246 nm). In such domains, the STS data (Fig. S2-d [50]) reveal a bandgap of about 1.90 eV, in agreement with previous works [51, 52, 53]. The valence band maximum (VBM) and conduction band minimum (CBM) are located close to -1.65 eV below and +0.25 eV above the Fermi level respectively. All the 1L PtSe₂ domains probed in this work are featureless and have the same apparent height when imaged at +1.2V sample bias, this is about 1 eV above the CBM, as shown in Fig. 1-a and Fig. S1 [50]. However, when the sample bias is set inside the 1L PtSe₂ gap as in Fig. 1-b, or close to the VBM as in Fig. S3-b or in Fig. S5-a [50], their appearance changes remarkably. Triangular superstructures with periods P in the nm range appear inside the islands, whose apparent height depends on the value of P . "Large" (≥ 1 nm) values of P correspond to apparently higher islands. Height differences of the order of 0.1 nm are measured between domains with different periods as shown in Fig. 1-c and Fig. S3-c [50]. In the data taken at a sample bias of +1.2V sample, tunneling occurs mainly towards empty states of 1L PtSe₂, and the images should represent the topography of this layer. Conversely, for sample bias within the TMD gap, the images should reflect the electronic structure of the 1L PtSe₂-BLG interface. Since free-standing 1L PtSe₂ has no states in this energy range, the electron states that contribute to the tunneling current within the TMD gap must originate mostly from those of the underlying BLG substrate, perturbed by the contact with 1L PtSe₂. One can illustrate how the BLG states are modified at the interface by considering the current vs. voltage ($I_t(V_s)$) spectra shown in Figure 1-d. The pink curve shows the spectrum measured on the bare BLG. When the tip is moved onto the 1L TMD domains, hence retracted by roughly 0.8 nm (ie by the apparent height of the layer at the bias set point of +1.2V), a significant current is still measured within the TMD bandgap (light and dark blue curves respectively), 4 to 5 order of magnitude higher than expected for an attenuation 'as in vacuum' of the tunneling current into the BLG states (Section SI3 of Ref. [50]). This implies that the graphene derived states gain an extra spectral weight within the TMD layer in the energy range of the bandgap, thus that they acquire a partial PtSe₂ character. Otherwise stated, there is a finite, albeit small, admixture of states originating from PtSe₂ into the mainly graphene-based in-gap states (Section SI3 in Ref. 50). This is a strong indication for the existence of hybridized Graphene-PtSe₂ electron states

within the TMD bandgap. The experimental variations of the $I_t(V_s)$ curves between the two islands in Fig. 1-d and Fig. S3-d, or equivalently the variations of the apparent height of the islands in images taken with sample biases within the gap (Fig. 1-b and S3-b), indicate that the admixture of PtSe₂ derived states depends on the value of P. The larger current or apparent height for long period ($P \geq 1$ nm) superstructures suggests that the hybridization should be stronger in this case.

Ab initio band structure calculations confirm the existence of such hybridized states at the BLG-1L PtSe₂ bilayer, as shown in Fig. 1-e and 1-f (see also Fig. S11 [50]). The atomic lattices of BLG and PtSe₂ are aligned for this calculation. Therefore, due to the (3x3) BLG supercell used, both +K and -K points of the Brillouin zone (BZ) of BLG are backfolded at Γ . The calculated band structure of the heterostructure is projected on the BLG and on the PtSe₂ layers in Fig. 1-e and Fig. 1-f respectively. Within the TMD bandgap at Γ (and even up to +0.75 eV) one clearly recognizes the characteristic band structure of bare BLG in Fig. 1-e (heavy red line). The same features are found, although with a much smaller weight, in Fig. 1-f (light blue lines inside the pink rectangle). This calculation shows that, inside the TMD bandgap, the eigenstates, which mainly originate from the bare BLG states, acquire a small weight on the orbitals of the Pt and Se. Therefore, hybrid states with a small admixture of PtSe₂ form within the bandgap at the TMD/BLG interface. Similar results were found for the interface between 1L PtSe₂ and monolayer graphene, see Fig. S11.

In Ref. 50 (section SI4) we show that the period (P) of the triangular superstructures observed inside the 1L-PtSe₂ islands is related to the rotation angle θ between the crystallographic directions of the 1L PtSe₂ and of the BLG substrate. The value of θ can be evaluated directly from images with atomic resolution on the bare BLG and on the TMD islands (Fig. S5 [50]). The superstructures are thus Moiré Patterns (MPs) resulting from this disorientation. Figure 2-a, 2-c and 2-e show atomic resolution images of domains with different values of θ . Their Fourier transforms (FTs) are displayed in Figure 2-b, 2-d and 2-f. For the aligned domain with $\theta = 0^\circ$ (Fig. 2-a and 2-b) one identifies readily the (2x2) superstructure. The first order spots of the superstructure are labelled as "MP1" (pink triangles) in Fig. 2-b. Strong second order spots, indicated by the white arrows, are also present. For a small but finite rotation angle $\theta \approx 4^\circ$, the real space image (Fig. 2-c) becomes more complex. The corresponding FT (Fig. 2-d) reveal two sets of spots, marked as MP1 (pink triangles) and MP2 (orange triangles), both corresponding to the superstructure. We ascribe the spots labelled MP1 to a Moiré pattern based on the difference between the (shortest) reciprocal vectors of PtSe₂ and of the graphene lattices [54, 55], as shown in Fig. 2-g. It coincides with the (2x2) superstructure for $\theta = 0^\circ$. The second series of spots, labelled MP2, also corresponds to a MP constructed on the difference between the reciprocal vector of graphene (\mathbf{a}^*_{Gr}) and the sum of the reciprocal vectors of PtSe₂ ($\mathbf{a}^*_{TMD} + \mathbf{b}^*_{TMD}$) lattices, see Fig. 2-g (plus symmetry related vectors). It coincides with the second order spots of the (2x2) superstructure for $\theta = 0^\circ$ (white arrows in Fig. 2-b). For large rotation angles ($\theta \approx 20^\circ$, Fig. 2-e and 2-f) we identify one set of spots which correspond to the MP2 Moiré pattern. The computed variations of the structural parameters of MP1 and MP2 as functions of θ are displayed in Fig. S9. We find a good agreement between the period and the orientation of the superstructures obtained from the analysis of the FTs of the images and the values computed from the direct measurement of θ . Additional data on that point are presented in Ref. 50. These observations strongly support our interpretation of the superstructure in terms of those two Moiré patterns (MP1 and MP2). A very important point for the purpose of the present work is that MP2 is detected for all values of θ (assuming that the second order spot of the (2x2) for $\theta = 0^\circ$ correspond to MP2). Figures 2, S7 and S8 suggest that MP1 is strongly attenuated for $\theta \geq 9^\circ$, especially at large negative bias, whereas MP2 is present at any angle and for all sample biases. The occurrence of the Moiré MP1 in our STM images is considered in section SI5 of Ref. 50, but it is not relevant for the following discussion.

Our experimental data therefore suggest the following picture for the electronic structure of the interface. Graphene (BLG) π states located within the bandgap of the TMD interact with the TMD potential, which gives rise to hybrid states having a partial PtSe₂ character. This “in-gap” PtSe₂ contribution, as probed by the STM tip, (i) shows ubiquitous spatial modulations related to the so-called MP2 moiré pattern and (ii) depends on the rotation angle between the TMD and BLG substrate, being larger for large rotation angles. Actually, these observations are consistent with the scenario proposed for the interlayer interaction at an (arbitrary) incommensurate interface [36]. This mechanism has been adapted to the case of a semiconducting TMD-graphene interface in the context of the proximity effect [28, 29]. Even though single layer graphene is considered in Ref. [28, 29], the same discussion should hold in the BLG case. The low energy states of graphene, those which are present within the 1L PtSe₂ bandgap, are located close to the K_G (and $-K_G$) points of the graphene Brillouin zone (BZ). From Ref. [28, 29], each graphene state is coupled essentially with TMD states located at three points in the first Brillouin zone of 1L PtSe₂, following the momentum conservation rule [36]. This mechanism is illustrated in Figure 3-a to 3-c for different rotation angles in the case of graphene states located close to the K_G point [28, 29] (the same arguments hold for the $-K_G$ point). Therefore, the hybrid interface states within the gap consist of a sum of a (dominant) graphene contribution and of a set of 1L PtSe₂ states with wave vectors \mathbf{k}_1 , \mathbf{k}_2 and \mathbf{k}_3 in the 1L PtSe₂ first BZ (see Fig. 3). As shown in figure S10 [50], those three wave-vectors are connected by reciprocal vectors of the MP2 Moiré pattern. Consequently, for any value of θ , the squared wavefunction of each hybrid state, evaluated in the 1L PtSe₂ layer (i. e. disregarding the graphene component) will contain terms oscillating with the periodicity of MP2. The result is consistent with our observation of the MP2 superstructure for all orientations of the TMD layer.

Moreover, considering that a graphene state located within the bandgap can be rather far (a fraction of an eV) from the band edges of the TMD, the related hybrid state can be obtained from perturbation theory [28, 29]. The amplitude of the 1L PtSe₂ contributions to the hybrid state will be proportional to a matrix element and inversely proportional to the distance in energy between the graphene and the 1L PtSe₂ states with wavevectors \mathbf{k}_1 , \mathbf{k}_2 or \mathbf{k}_3 [29]. This provides an explanation for the angular variation of the weight of the 1L PtSe₂ contribution within the gap which is observed experimentally. Indeed, as shown in Figure 3, graphene states at the K_G point will be coupled to different states \mathbf{k}_i ($i=1$ to 3) in the PtSe₂ layer when the rotation angle changes. One reason of the angular variation of the PtSe₂ weight could be that the TMD states have different Pt and Se orbital character for different values of θ [41, 52], which will modify the value of the matrix element. This effect is not intuitive and it has to be computed numerically [28, 29]. The other reason, which is the role of the distance in energy between graphene and TMD states, can be more readily evaluated considering the calculated band structure of freestanding 1L PtSe₂ (see Fig. 3-d), as shown in Ref. 29. The values of the vectors \mathbf{k}_i of the TMD states hybridized with the graphene states at the K_G point (DP) are indicated for specific values of θ in Fig. 3-d (cf. Ref. 50 for technical remarks on this figure). From the calculation of the heterojunction (TMD on BLG, see Fig 1-e and 1-f and S11), the DP of BLG is 0.4 eV below the CBM, this is close to E_F in Fig. 3-d. One can thus see from Fig. 3-d that the distance in energy between a graphene state located at the K_G point (DP) and the \mathbf{k}_1 , \mathbf{k}_2 and \mathbf{k}_3 1L PtSe₂ states changes markedly with θ (roughly by a factor of 2). This modifies the amplitude of the 1L PtSe₂ contributions to the hybrid state in the perturbative approach. Considering only this effect, one expects a weak amplitude for small values of θ (around 0°) and a stronger one for larger values of θ (around 25-30°). In the experiments, the DP of graphene is located 0.30 eV below the Fermi level [35, 50], this is 0.55 eV below the CBM [50]. The coupling of the graphene states close to the DP to the ones of the 1L PtSe₂ layer should thus follow the same trends as in the calculations. Therefore, we can infer that the in-gap tunneling current, or the apparent height of the islands for in-gap imaging biases, should be smaller for small angles ($\theta \approx 0^\circ$, $P < 1$ nm) than for larger ones ($\theta \geq 20^\circ$, $P \geq 1$ nm). This is in agreement with the experimental observations reported in Figures 1

and S3 [50], and supports the interpretation of these data in terms of hybridized states at the interface. However, considerations based only on the energy separation of the bands may be insufficient to fully describe the complexity of the systems, as revealed by ab initio studies [30, 31, 32]. It was suggested that band anticrossings may be a better way to evaluate the coupling between graphene and TMD states [32]. We address this point in Ref. 50 (section SI6, Fig. S12) for the specific case $\theta=19.1^\circ$. Our ab-initio calculations also support a larger hybridization for this rotation angle than for $\theta=0^\circ$.

In summary, our experimental study of the 1L PtSe₂-BLG junction, supported by ab initio calculations, has revealed the salient features of the interlayer interaction between the states in this twisted van der Waals heterostructure. This was achieved by analyzing the electronic states appearing inside the TMD bandgap as a result of hybridization at the interface. The momentum conservation rule gives rise to a specific Moiré pattern observed in the whole range of rotation angles. The angular dependence of the coupling strength between the layers gives rise to variations in the tunneling current measured in the TMD bandgap. Beyond the case of the 1L PtSe₂-BLG system, our work supports theoretical [28-32] models which propose to use the twist angle as a knob to tune the amplitude of the proximity effect in SC TMD-graphene junctions.

References:

- [1] I. Zutic, A. Matos-Abiague, B. Scharf, H. Dery, K. Belaschhenko, *Mater. Today* **22**, 85 (2019).
- [2] K. S. Novoselov, A. Mishchenko, A. Carvalho, A. H. Castro Neto, *Science* **353**, 461 (2016)
- [3] J. H. Garcia, M. Vila, A. W. Cummings and S. Roche, *Chem. Soc. Rev.* **47**, 3359 (2018)
- [4] J. F. Sierra, J. Fabian, R. K. Kawakami, S. Roche, S. O. Valenzuela, *Nat. Nanotechnol.* **16**, 856 (2021)
- [5] A. Avsar, J.Y. Tan, T. Taychatanapat, J. Balakrishnan, G.K.W. Koon, Y. Yeo, J. Lahiri, A. Carvalho, A.S. Rodin, E.C.T. O'Farrell, G. Eda, A.H. Castro Neto and B. Özyilmaz, *Nat. Commun.* **5**:4875 (2014)
- [6] Z. Wang, D.-K. Ki, Hua Chen, H. Berger, A. H. MacDonald and A. F. Morpurgo, *Nat. Commun.* **6**:8339 (2015)
- [7] M. Gmitra, D. Kochan, P. Högl, and J. Fabian, *Phys. Rev. B* **93**, 155104 (2016)
- [8] M. Offidani, M. Milletari, R. Raimondi, and A. Ferreira, *Phys. Rev. Lett.* **119**, 196801 (2017)
- [9] M. Gmitra and J. Fabian, *Phys. Rev. Lett.* **119**, 146401 (2017)
- [10] Z. Wang, D.-K. Ki, J. Y. Khoo, D. Mauro, H. Berger, L. S. Levitov, and Alberto F. Morpurgo, *Phys. Rev. X* **6**, 041020 (2016)
- [11] B. Yang, M. Lohmann, D. Barroso, I. Liao, Z. Lin, Y. Liu, L. Bartels, K. Watanabe, T. Taniguchi, and J. Shi, *Phys. Rev. B* **96**, 041409(R) (2017)
- [12] S. Zihlmann, A. W. Cummings, J. H. Garcia, M. Kedves, K. Watanabe, T. Taniguchi, C. Schönenberger, and Péter Makk, *Phys. Rev. B* **97**, 075434 (2018)
- [13] S. Omar and B. J. van Wees, *Phys. Rev. B* **97**, 045414 (2018)
- [14] T. Wakamura, F. Reale, P. Palczynski, S. Guéron, C. Mattevi, and H. Bouchiat, *Phys. Rev. Lett.* **120**, 106802 (2018)

- [15] L. Benítez, J. F. Sierra, W. Savero Torres, A. Arrighi, F. Bonell, M. V. Costache and S. O. Valenzuela, *Nature Phys.* **14**, 303 (2018)
- [16] D. Wang, S. Che, G. Cao, R. Lyu, K. Watanabe, T. Taniguchi, C. Ning Lau, and M. Bockrath, *Nano Lett.* **19**, 7028 (2019)
- [17] H. X. Yang, A. Hallal D. Terrade, X. Waintal, S. Roche, and M. Chshiev, *Phys. Rev. Lett.* **110**, 046603 (2013)
- [18] K. Zollner, M. Gmitra, T. Frank, and J. Fabian, *Phys. Rev. B* **94**, 155441 (2016)
- [19] K. Zollner, M. Gmitra and J. Fabian, *New J. Phys.* **20**, 073007 (2018)
- [20] S. K. Behera, M. Bora, S. Sindhu, P. Chowdhury and P. Deb, *Phys. Chem. Chem. Phys.* **21**, 25788 (2019)
- [21] C. Tang, Z. Zhang, S. Lai, Q. Tan, and Wei-bo Gao, *Adv. Mater.* **32**, 1908498 (2020)
- [22] T. S. Ghiasi, A. A. Kaverzin, A. H. Dismukes, D. K. de Wal, X. Roy and Bart J. van Wees, *Nature Nanotech.* **16**, 788 (2021)
- [23] Y. Wu, G. Yin, L. Pan, A. J. Grutter, Q. Pan, A. Lee, D. A. Gilbert, J. A. Borchers, W. Ratcliff II, A. Li, X.-dong Han and K. L. Wang, *Nature Electronics* **3**, 604 (2020)
- [24] B. Karpiak, A. W Cummings, K. Zollner, M. Vila, D. Khokhriakov, A. Md Hoque, A. Dankert, P. Svedlindh, J. Fabian, S. Roche and S. P Dash, *2D Mater.* **7**, 015026 (2020)
- [25] F. Ibrahim, A. Hallal, D. Solis Lerma, X. Waintal, E. Y. Tsymbal and M. Chshiev, *2D Materials* **7**, 015020 (2020)
- [26] W. Han, R. K. Kawakami, M. Gmitra, M. and J. Fabian, *Nature Nanotech.* **9**, 794 (2014).
- [27] H. Yang, S. O. Valenzuela, M. Chshiev, S. Couet, B. Dieny, B. Dlubak, A. Fert, K. Garello, M. Jamet, D.-E. Jeong, K. Lee, T. Lee, M.-B. Martin, G. S. Kar, P. Sénor, H.-J. Shin and S. Roche, *Nature* **606**, 663 (2022)
- [28] A. David, P. Rakyta, A. Kormányos, and G. Burkard, *Phys. Rev. B* **100**, 085412 (2019)
- [29] Yang Li and M. Koshino, *Phys. Rev. B* **99**, 075438 (2019)
- [30] T. Naimier, K. Zollner, M. Gmitra and J. Fabian, *Phys. Rev. B* **104**, 195156 (2021)
- [31] A. Pezo, Z. Zanolli, N. Wittemeier, P. Ordejón, A. Fazzio, S. Roche and J. H Garcia, *2D Mater.* **9**, 015008 (2022)
- [32] K. Zollner and J. Fabian, *Phys. Rev. Lett.* **128**, 106401 (2022)
- [33] E. Y. Andrei, D. K. Efetov, P. Jarillo-Herrero, A. H. MacDonald, K. F. Mak, T. Senthil, E. Tutuc, A. Yazdani and A. F. Young, *Nature Rev. Mater.* **6**, 201 (2021).
- [34] Ado Jorio, *Nature Mater.* **21**, 844 (2022)
- [35] P. Mallet, I. Brihuega, S. Bose, M. M. Ugeda, J. M. Gómez-Rodríguez, K. Kern, and J. Y. Veuillen, *Phys. Rev. B* **86**, 045444 (2012)
- [36] Mikito Koshino, *New J. Phys.* **17**, 015014 (2015)

- [37] L. Sun, L. Rademaker, D. Mauro, A. Scarfato, Á. Pásztor, I. Gutiérrez-Lezama, Z. Wang, J. Martinez-Castro, A. F. Morpurgo and C. Renner, *Nature Comm.* **14**:3771 (2023)
- [38] Y. Zhao , J. Qiao , P. Yu , Z. Hu , Z. Lin , S. Ping Lau , Z. Liu , W. Ji and Y. Chai, *Adv. Mater.* **28**, 2399 (2016)
- [39] A. Ciarrocchi, A. Avsar, D.Y. Ovchinnikov and A. Kis, *Nature Comm.* **9**:919 (2018)
- [40] R. A. B. Villaos, C. P. Crisostomo, Z.-Q. Huang, S.-M. Huang, A. A. B. Padama, M. A. Albao, H. Lin and F.-C. Chuang, *npj 2D Materials and Applications* **3**:2 (2019)
- [41] W. Yao, E. Wang, H. Huang, Ke Deng, M. Yan, K. Zhang, K. Miyamoto, T. Okuda, L. Li, Y. Wang, H. Gao, C. Liu, W. Duan and S. Zhou, *Nature Comm.* **8**, 14216 (2017)
- [42] M. Kurpas and J. Fabian, *Phys. Rev. B* **103**, 125409 (2021)
- [43] K. Abdukayumov, M. Micica, F. Ibrahim, C. Vergnaud, A. Marty, J.-Y. Veuillen, P. Mallet, I. de Moraes, D. Dosenovic, A. Wright, J. Tignon, J. Mangeney, A. Ouerghi, V. Renard, F. Mesple, F. Bonell, H. Okuno, M. Chshiev, J.-M. George, H. Jaffrès, S. Dhillon and M. Jamet, arXiv:2305.06895v1
- [44] A. Avsar, C.-Y. Cheon, M. Pizzochero, M. Tripathi, A. Ciarrocchi, O. V. Yazyev and A. Kis, *Nature Comm.* **11**:4806 (2020)
- [45] P. Mallet, F. Varchon, C. Naud, L. Magaud, C. Berger and J.-Y. Veuillen, *Phys. Rev. B* **76**, 041403(R) (2007)
- [46] I. Horcas, R. Fernández, J. M. Gómez-Rodríguez, J. Colchero, J. Gómez-Herrero, A. M. Baro, *Rev. Sci. Instrum.* **78**, 013705 (2007)
- [47] G. Kresse and J. Hafner, *Phys. Rev. B* **47** , 558 (1993); *ibid.* **49** , 14 251 (1994)
- [48] G. Kresse and J. Furthmuller, *Comput. Mat. Sci.* **6** , 15 (1996)
- [49] G. Kresse and J. Furthmuller, *Phys. Rev. B* **54** , 11 169 (1996)
- [50] See Supplementary informations for details on sample preparation, ab-initio calculations and STM set-up. This Supplementary information provides additional data complementing those of Figure 1 to Figure 3 in the main text.
- [51] Xu Wu, Jingsi Qiao, Liwei Liu, Yan Shao, Zhongliu Liu, Linfei Li, Zhili Zhu, Cong Wang, Zhixin Hu, Wei Ji, Yeliang Wang and Hongjun Gao, *Nano Res.* **14**, 1390 (2021)
- [52] Lei Zhang, Tong Yang, Muhammad Fauzi Sahdan, Arramel, Wenshuo Xu, Kaijian Xing, Yuan Ping Feng, Wenjing Zhang, Zhuo Wang and Andrew T. S. Wee, *Adv. Electron. Mater.* **7**, 2100559 (2021)
- [53] Jingfeng Li, Sadhu Kolekar, Mahdi Ghorbani-Asl, Tibor Lehnert, Johannes Biskupek, Ute Kaiser, Arkady V. Krashennnikov, and Matthias Batzill, *ACS Nano* **15**, 13249 (2021)
- [54] I. Amidror, "The Theory of the Moiré Phenomenon", Kluwer Academic Publishers, The Netherlands (1999)
- [55] F. Hiebel, P. Mallet, L. Magaud, and J.-Y. Veuillen, *Phys. Rev. B* **80**, 235429 (2009)

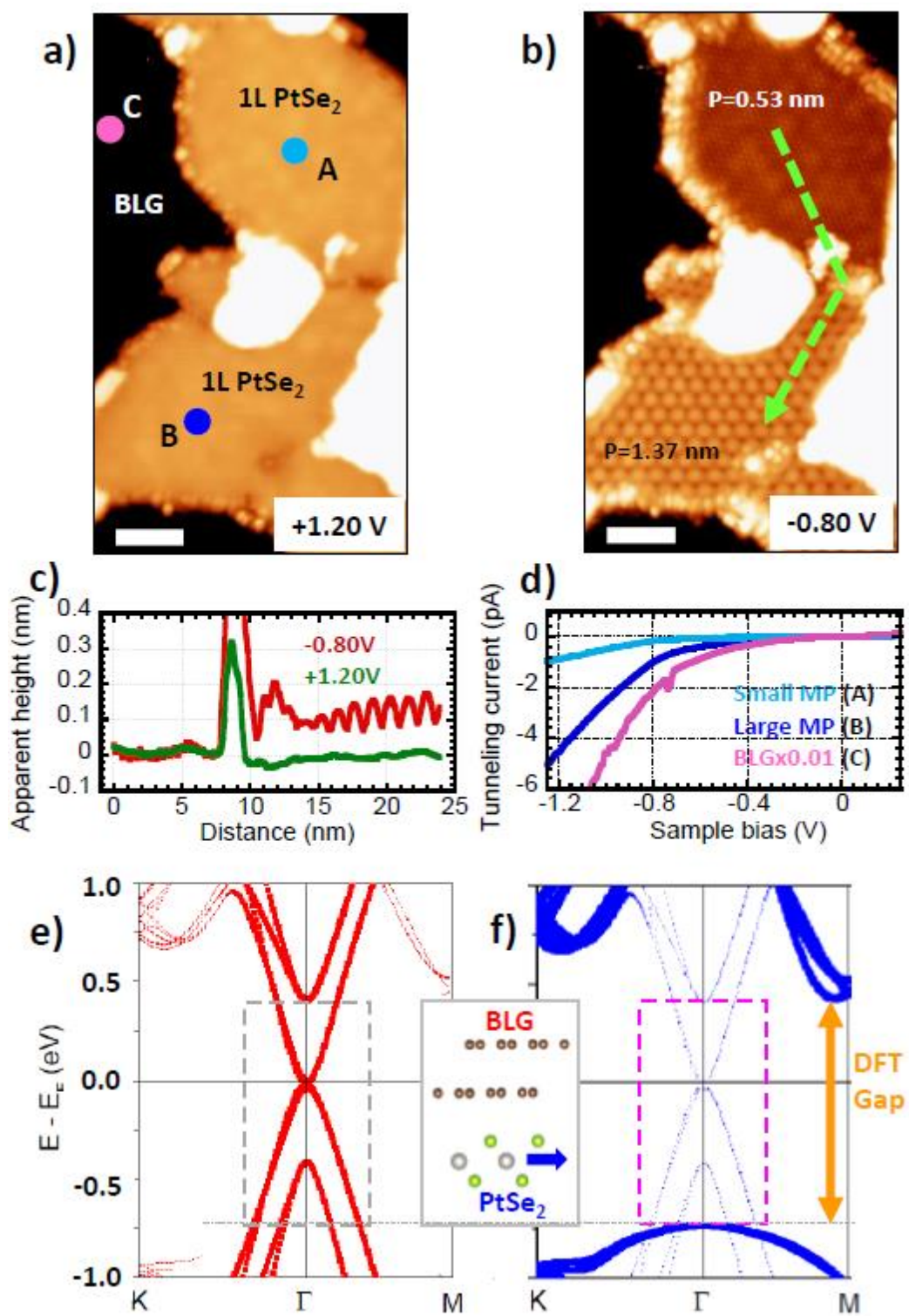


Figure 1

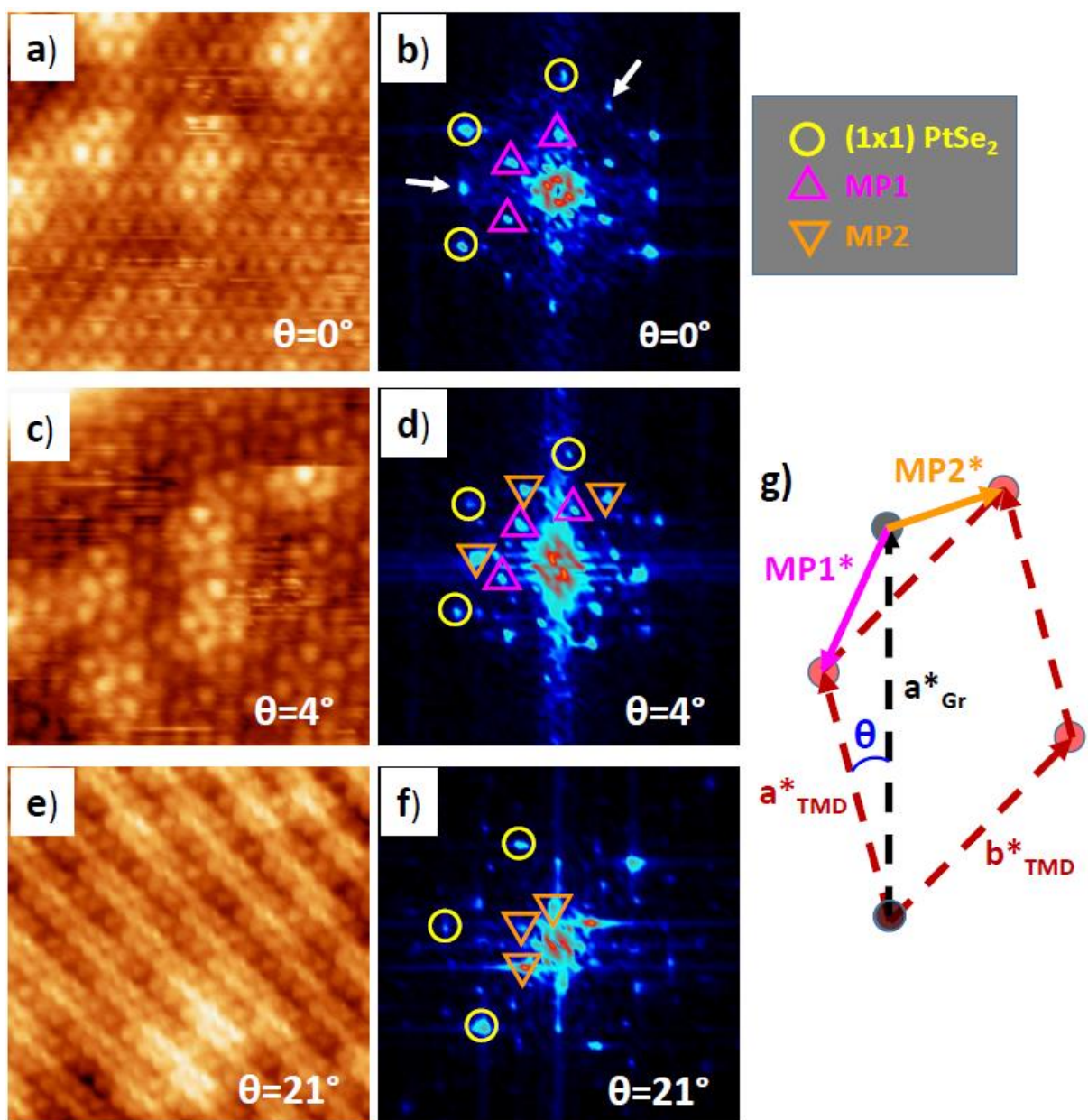


Figure 2

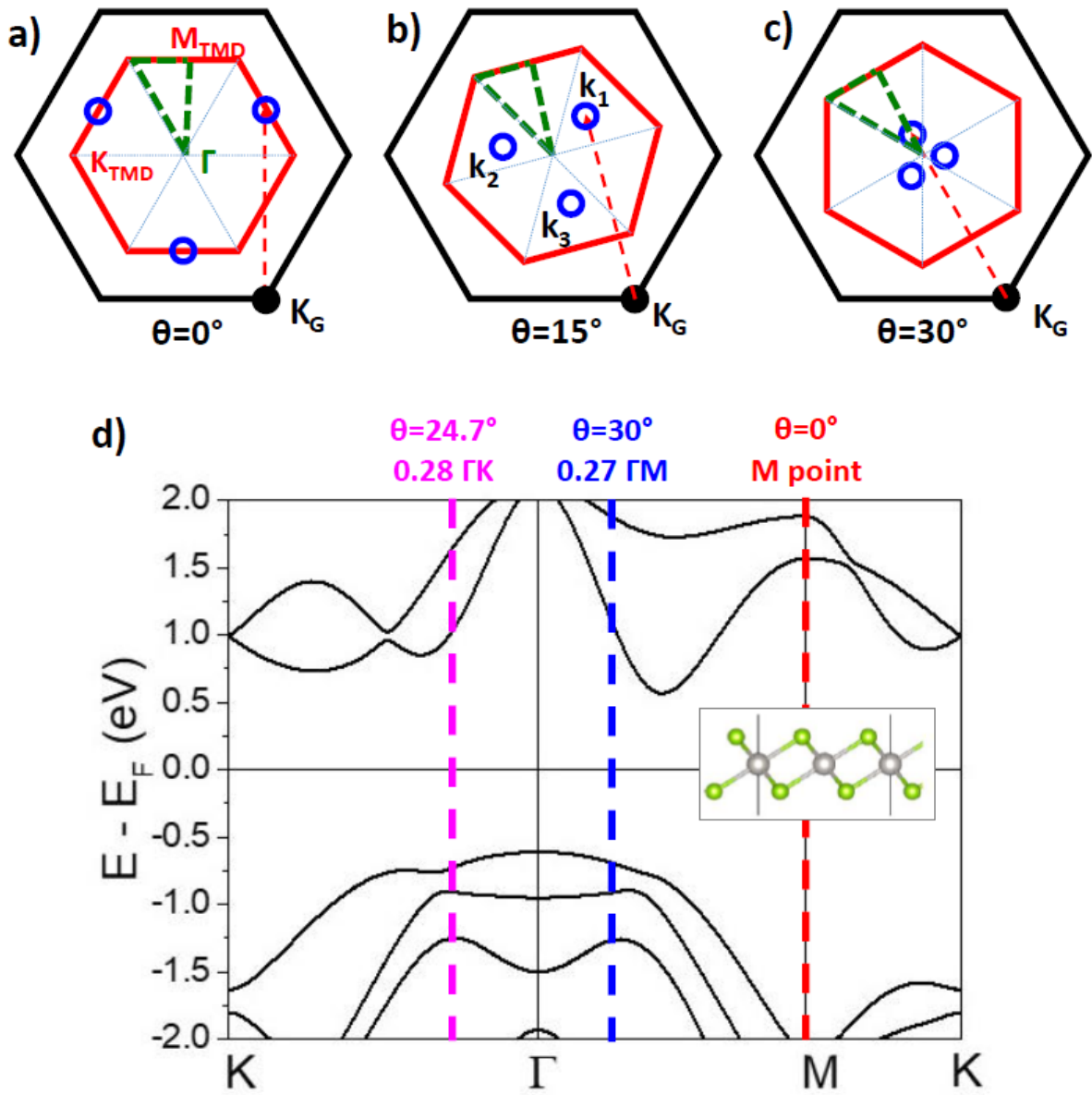


Figure 3

Figure captions:

Figure 1: Superstructures at the interface between 1L PtSe₂ and BLG. a) Constant current STM image taken with sample bias $V_s=+1.20$ V and tunneling current $I_t=20$ pA. The scale bar is 5 nm. b) Image of the same area with $V_s=-0.80$ V and $I_t=5$ pA. The periods of the superstructures that appear in the upper (lower) island are 0.53 nm (1.37 nm). c) Profile of the apparent height taken on images in a) and b) along the path represented by a broken line in b). d) Tunneling spectra ($I_t(V_s)$ curves) taken at the point labelled A (light blue curve), B (dark blue curve) and C (pink curve, on the BLG) in a). The set-point for all spectra was $V_s=+1.20$ V and $I_t=500$ pA. The value of the current on the BLG is divided by 100 in the plot. e) and f) Calculated electronic structure for the interface between 1L PtSe₂ and BLG. The relaxed structure of the system is displayed in the central panel. The atomic lattices of BLG and 1L PtSe₂ are aligned (i. e. $\theta=0^\circ$), and the common (commensurate) unit cell is (2x2) PtSe₂ or (3x3) BLG. The band structure of the heterojunction is projected on the BLG in red (e) and on the 1L PtSe₂ layer in blue (f) respectively. The size of the symbols (dots) in the plots is proportional to the weight of the site-projected state in the corresponding layer. The orange arrow in f) indicates the calculated TMD bandgap. The pink rectangle in f) indicates the location where hybridized states appear within the TMD bandgap (a grey rectangle is shown at the same position in e)).

Figure 2: Superstructures as Moiré patterns. a), b) and c): Constant current images with size 6x6 nm² taken on domains with different values of the twist angle θ . $V_s=-1.80$ V for a) and c), $V_s=+0.10$ V for e). Images for other biases are shown in Fig. S8 [49]. b), d) and f): FTs of the images in a), c) and e) respectively. The first order spots of the reciprocal lattice of 1L PtSe₂ are indicated by yellow circles. The spots corresponding to the Moirés patterns MP1 and MP2 are indicated by pink and orange triangles respectively. g) Construction giving the reciprocal lattice vectors of the Moiré patterns MP1 and MP2 [53, 54]. a^*_{TMD} and a^*_{Gr} are the reciprocal vectors of the 1L PtSe₂ and BLG lattices respectively.

Figure 3: Hybridization of the graphene and TMD states at the interface. a), b) and c): Locations in the first Brillouin zone (BZ) of 1L PtSe₂ of the wavevectors of the TMD states coupled to the low energy BLG states for different rotation angles θ ($\theta=0^\circ$ in a), $\theta=15^\circ$ in b) and $\theta=30^\circ$ in c)). The BZ of BLG (1L PtSe₂) are drawn in black (red) lines respectively. The construction [28, 29] that gives the wavevector k_1 of the TMD layer coupled to the BLG states close to K_G is illustrated in a) to c), where the dashed red arrow represents a reciprocal lattice vector of 1L PtSe₂. k_2 and k_3 are obtained from the other equivalent K_G points in the BLG BZ. d): Location of the k_i ($i=1$ to 3) for states relative to the graphene Dirac point in the calculated band structure of freestanding 1L PtSe₂. The dashed vertical lines indicate the values of the k_i 's for specific rotation angles, where they cross the main directions (ΓM , ΓK or $K M$) of the BZ of 1L PtSe₂.

Acknowledgements:

The authors acknowledge the support from European Union's Horizon 2020 research and innovation Programme under grant agreement No 881603 (Graphene Flagship) and from the French National Research Agency (ANR) through the ANR-18-CE24-0007 MAGICVALLEY project.